Fast Drying and Film Formation of Latex Dispersions Studied with FTIR Spectroscopic Imaging

James A. Kimber,[†] Matthias Gerst,[‡] and Sergei G. Kazarian[*,†]

Department of Chemical Engineering, Imperial College London, London, SW7 2AZ, United Kingdom, and BASF Advanced Chemicals Co., Ltd., GMU/SD, 300 Jiang Xin Sha Road, Pudong Shanghai 200137, P. R. China

E-mail: s.kazarian@imperial.ac.uk

Abstract

Drying of thin latex films (≈20 µm) at high drying speeds (of the order of seconds) has been studied by fast chemical imaging. ATR-FTIR spectroscopic imaging combined with a fast "kinetic" mode was used to acquire spectral images without co-addition, enabling the amount of water and homogeneity of drying film to be studied over time. Drying profiles, constructed from analysing the water content in each image, show two stages of drying, a fast and a slow region. The formulation of latex dispersions affects the onset of slow drying and the volume fraction of water remaining at the onset of slow drying. In this work, the effect of physical properties, film thickness and glass transition temperature (T_g), were investigated, as well as the effect of monomer composition where two monomoers, 2-Ethylhexylacrylate (EHA) and

[*]To whom correspondence should be addressed

[†]Department of Chemical Engineering, Imperial College London, London, SW7 2AZ, United Kingdom

[‡]BASF Advanced Chemicals Co., Ltd., GMU/SD, 300 Jiang Xin Sha Road, Pudong Shanghai 200137, P. R. China

nButylacrylate (nBA) and the amount of hydrophilic comonomer, Methylmethacrylate (MMA) were varied. It was found that thicker films produced slower overall drying, and that the formulation with a T_g above the minimum film formation temperature (MFFT) did not dry evenly, exhibiting cracking. However, the drying kinetics of high and low T_g films were similar, highlighting the advantage of using a spatially-resolved spectroscopic approach. Formulations containing more MMA dried faster than those with less. This was due to the hydrophilicity of MMA and the increase in T_g of the dispersion from the addition of MMA. Overall, FTIR spectroscopic imaging was shown to be a suitable approach in measuring film drying at high speeds as both chemical changes and chemical distribution could be analysed over time.

Introduction

Latex, or more generally, colloidal or polymeric dispersions, are a colloidal suspension of polymer particles typically between 1 nm and 1 µm. The synthesis of latex dispersions is often accomplished using emulsion polymerisation in which monomers such as acrylates, are emulsified in solution containing surfactant and polymerisation initiators.[1,2] The application of latex dispersions is common for paints and adhesives, and the use of water-based dispersions is environmentally advantageous over those employing organic solvents. During latex film formation, the solvent evaporates, latex particles pack, deform and eventually coalesce. The latter stages of particle deformation coalescence is particularly important in obtaining a homogeneous, optically transparent film. Depending on the latex composition (e.g. main monomer, co-monomer, solvent and surfactant), temperature of drying and the rate at which water evaporation occurs, different qualities of films are obtained. For example, drying at temperatures below the minimum film formation temperature (MFFT), particles will not coalesce, resulting in a brittle or powdery film, whereas when drying above the glass transition temperature (T_g), molecular chains diffuse between the latex particles, resulting in a continuous polymer film. In some cases, the stages of film formation may occur at

different times within the film. At high drying temperatures where water evaporation is very fast, particles at the surface may coalesce to form a film, trapping water below and hindering subsequent drying. In these cases, applying higher drying temperatures can result in slower film drying. The mechanisms of film formation along with methods in which they are analysed have been extensively reviewed.[3–6] In this paper, particular interest is paid to the formation of thin latex films at high temperatures as this most closely matches conditions in industrial coating applications. Assessing film formation over time under industrially relevant conditions is challenging due to the high mass transfer rates involved. Cryogenic Scanning Electron Microscopy (SEM), where films are quenched at various points throughout drying and studied using SEM, reveals the spatial distribution of latex particles and where coalescence has occurred.[7] Advances in SEM such as Environmental Scanning Electron Microscopy (ESEM)[8] or Wet Scanning Tunneling Electron Microscopy[9] allow in-situ drying to be studied, although this must still occur under vacuum conditions. Conventional NMR,[10] or Gradient At Right-angles to the Field or GARField, have been used to study the water content within a drying film[11] as well as cross-linking[12] and spectroscopic approaches such as Inverse-Micro-Raman-Spectroscopy[13] and infrared microscopy[14] have provided further insight into the distributions of polymer and water during drying. These approaches average over a volume of the film in the case of conventional NMR, give insight into one dimension in the case of GARField, or are point-based (infrared microscopy and Raman) and thus require a degree of mapping in order to probe different parts of the film as it dries. When drying proceeds slowly compared to the time required to map regions of interest, the film can be assumed to be in a pseudo-steady state condition during these times. However, for faster drying speeds (i.e. seconds), it would not be possible to map a line or area within the time frame.

Attenuated Total Reflection Fourier Transform Infrared (ATR-FTIR) has been applied to study dynamic processes such as crystallization of droplets,[15] latex film formation,[16] with multi-bounce ATR offering insight at both the film-air interface and the film-substrate

interface[17] and this technique has also been used to measure latex binder migration upon drying.[18] Recent advances in computational speed and the introduction of infrared array detectors enable film formation to be studied at high temperatures and speeds while retaining chemical specificity and also providing spatial information without the use of mapping. Focal plane array detectors combined with ATR-FTIR spectrometers have been used to study a wide range of dynamic systems[19] such as pharmaceuticals,[20] biological systems[21] and protein crystallisation.[22] The key advantages of this imaging approach over in-situ mapping or quench-based approaches are that an area of the film can be monitored chemically and spatially as it dries quickly under high temperature air, with little interference or geometric constraints, other than the film drying on the impermeable ATR crystal surface. It thus allows a close approximation to drying conditions that would occur in industrial coaters. In this work, ATR-FTIR spectroscopic imaging is used to study thin film formation under industrially relevant conditions (fast drying speeds using high temperature air) and show the effects of changing formulation parameters on drying performance.

Experimental Section

FTIR spectroscopic imaging

FTIR spectroscopy relies on the absorbance of specific frequencies of infrared by a sample. These frequencies correspond to vibrational modes of different functional groups or chemical bonds within a sample and thus a spectrum (plot of absorbance against frequency) can be used to identify the components present in a system. The Lambert-Beer law can be used to relate absorbance of specific spectral bands to concentration, enabling quantitative information to be obtained. FTIR spectroscopic imaging combines conventional single-element FTIR spectroscopy with a Focal Plane Array (FPA) detector containing an array of 64 x 64 pixels. Each pixel resolves a full infrared spectrum simultaneously from different parts of the sample, enabling a variety of dynamic systems to be studied in a chemically specific

and spatially resolved manner. Combining FTIR imaging with an Attenuated Total Reflection (ATR) accessory (Specac diamond ATR Golden Gate^{TM}) accessory allows for strongly absorbing samples (aqueous suspensions etc.) to be studied with minimal preparation compared with transmission and is intrinsically non-destructive.[23,24] In ATR mode, an infrared beam undergoing total internal reflection within a suitably shaped crystal (commonly an inverted prism) will interact with a sample on the crystal surface via an evanescent wave. The evanescent wave exponentially decays as a function of distance from the surface and the depth of penetration, where the evanescent wave intensity falls to e^{-1} of the intensity at the surface, is dependent of wavelength, angle of incidence and the refractive index of the sample and crystal. For latex dispersions studied here, we assume the refractive index will be between 1.4 and 1.5, the angle of incidence is 45° and wavelengths used are between 2000 and 900 cm^{-1}, giving a depth of penetration between 0.8 and 2.2 µm. If quantitative measurements are required, is should be noted that as the film dries, the refractive index would increase, increasing the depth of penetration by approximately 7%. Determining the change in refractive index of a drying film can be derived by performing the same experiment on different ATR crystals and comparing changes in absorbance. The imaging area in this work was approximately 700 x 600 μm^2.

The diamond ATR accessory uses magnifying lenses, but this introduces multiple angles of incidence on the ATR crystal surface. To avoid possible gradient effects and anomalous dispersion, and maintain a well defined depth of penetration, an aperture was used on the condenser lens[25], restricting the angle of incidence to 45°.

Methodology

A heat gun was used to provide high temperature air to dry the latex film, where the distance between the ATR crystal and the heat gun nozzle was adjusted to control air temperature close to the ATR crystal (giving an air temperature of approximately 400 °C).

In order to deposit latex formulations consistently on the ATR crystal, a thin lead sheet

with a 5.5 mm hole, was placed on the tungsten carbide disk such that the hole was centrally aligned to the ATR crystal. Using a microlitre pipette, 2 to 3 µl, depending on the viscosity of formulation, was spread onto the ATR crystal. Prior to deposition, the heat gun was switched on to stabilise the air temperature out of the nozzle, and the spectrometer was instructed to start measuring. The latex formulation was then pipetted and spread within the lead ring over the ATR crystal, and immediately after three scans, the heat gun was placed over the sample at the required height. The images were measured in "kinetic" mode, where interferograms were acquired but not co-added and processed only after all scans were completed. The number of scans was set to 30, resulting in a series of spectral images approximately 1.011 seconds apart. The speed of acquisition depends on interferometer scanning speed, spectral resolution (in this work, $8\,\mathrm{cm}^{-1}$), spectral range ($2000\,\mathrm{cm}^{-1}$ to $900\,\mathrm{cm}^{-1}$, achieved using a low-pass filter) and FPA refresh rate. Further optimisation of these parameters can be used to acquire images of moving droplets at 50 ms intervals[26]. The spectrometer used in this work was a Bruker Equinox 55 with IMAC macrochamber. Images were generated from spectra by numerical integration of certain spectral bands. The carbonyl band between $1755\,\mathrm{cm}^{-1}$ and $1705\,\mathrm{cm}^{-1}$ was used to visualise the distribution of acrylic over time, and the bending mode of water between $1692\,\mathrm{cm}^{-1}$ and $1580\,\mathrm{cm}^{-1}$ was used to visualise water. The integration limits for these bands were chosen so as to minimise the influence from adjacent bands, while providing sufficient integral area to reduce the influence of noise, an important consideration since each spectrum is the result of one scan. The accuracy of this approach could be improved using multivariate analysis, which takes into account the whole spectrum rather than single spectral bands, further reducing the error from spectral noise and band overlap. In this work, the normalised change in the spectral band of the bending mode of water, is of primary interest, which is indicative of water loss within the drying film. Figure 1 shows schematically the set-up used and an example spectrum with band integration, used to produce the images.

The thickness and homogeneity of the resulting film was measured using a confocal

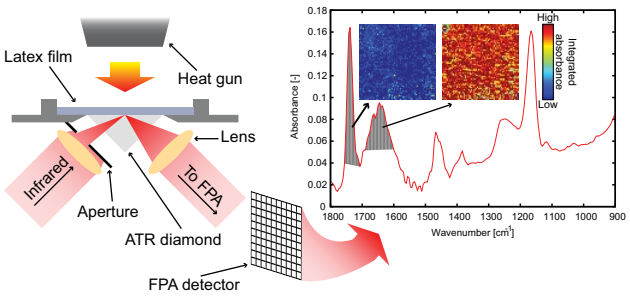

Figure 1: Schematic of film drying on the ATR crystal showing the aperture on the condenser lens and the generation of images from all spectra by spatially plotting the integrated absorbance of the bending mode of water (between 1692 cm^{-1} and 1580 cm^{-1}) or carbonyl band (between 1755 cm^{-1} and 1705 cm^{-1}) for water or polymer visualisation respectively.

microscope with an XYZ-motorized stage. The use of an internal aperture was used to visually assess focus on the surface of the film within an accuracy of ±2 µm. By scratching the dried film off part of the ATR crystal and focusing on this exposed part using the motorized stage, a read-out of the film thickness can be obtained. Depending on the amount of latex formulation initially deposited and how effectively it was spread, the target thickness was 20 µm to 24 µm.

Spectral image analysis

Average spectra from each image can be plotted as in Figure 2 showing the carbonyl band increasing and the bending mode of water band decreasing in intensity over time. Figure 2 also shows a typical set of images in a row, showing the polymer increasing in intensity and water decreasing as the formulation dries. The integrated absorbance values of the carbonyl and water bands from these average spectra can similarly be plotted over time, resulting in drying profiles. Normalisation of the profiles is based on the minimum and maximum integrated absorbance values averaged over the image, of each component, where it was observed from spectra that drying was complete within 25 seconds. In this work, the focus will be on the water loss over time and shall be referred to as the drying curve. In the ideal case, the profile would decrease to zero as quickly as possible. For drying of

latex dispersions, two stages are seen, a fast drying region, a plateau and a slow drying region towards the end. This correlates with similar studies in which two[27] or three[28] drying stages are proposed. In the case of three stages, the first is evaporation of water from the surface, causing latex particles to pack, the second stage occurs as the packed latex particles deform and the third is where polymer chains interdiffuse and the remaining water leaves the film either via capillaries or diffusing through the polymer itself. In two-stage drying, it is proposed that bulk water evaporates first, but in the second stage, a moving boundary occurs in the film where water evaporates from this boundary, percolating through the dry top layers. A comparison between the two theories has been extensively covered in review articles and compared with experiments or mathematical models.[5,29–31]

For comparison between latex compositions, the time between the application of heat and the start of slow drying can be defined as t_{fast} and the time between the onset of slow drying and the end of film drying can be defined as t_{slow}. At the point of slow drying, the normalised integrated absorbance of water will be some positive value, with lower values indicating less water in the film at the start of slow drying. This quantity is of interest as ideally, as much water as possible would be lost in the fast drying regime. As the dispersions contain the same volume fraction of water, it is possible to compare this value between formulations. To ascertain these values, a segmented polynomial with four control points was fitted to the data. The first point would be set to the maximum of the drying curve, the last point set to the first zero crossing point and the two intermediate points fitted to the drying curve so as to minimise the mean squared error of the fitted line with the data. The second point would be at the transition between fast and slow drying, and the third would be at the end of the plateau.

In cases of fast drying, latex particles can accumulate on the surface and can form a more or less dense skin, hindering the evaporation of water from below. The propensity for accumulation of particles depends on the drying rate as if the rate of evaporation is slower than the diffusion of the latex particles, a film will not be formed whereas in the reverse case,

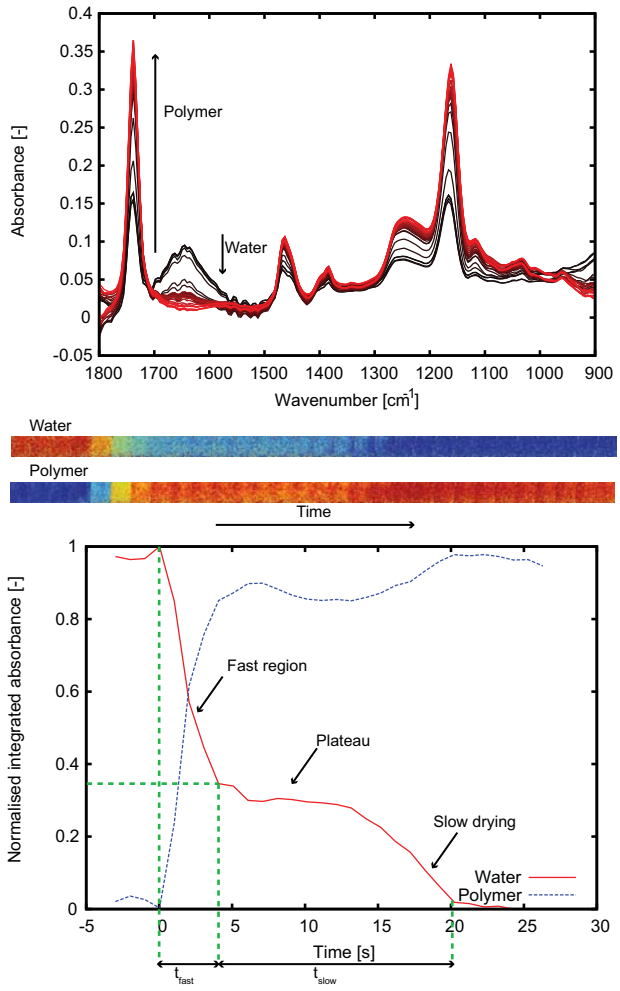

Figure 2: Average spectra from each image plotted over time (top) with example image strips (middle, each image is 700 x 600 µm^2) and plots of the average integrated absorbance for water and polymer in each image over time (bottom). The features of the drying curve, can be further defined as an initial fast drying region (t_{fast}), a plateau and a tail-off t_{slow}. The y-axis value where t_{fast} becomes t_{slow} is the fraction of water remaining with respect to the starting volume fraction of water. The latex dispersion used in this example contained 99% ethylhexylacrylate and 1% acrylic acid.

particles cannot redistribute or diffuse in time during evaporation of the water. The Peclet number can be used to express this mathematically in Equation 1, where H is the thickness of the film (m), E is the evaporation rate of water (ms^{-1}) and D_p is the diffusion coefficient of the latex particles (m^2s^{-1}).

$$Pe = \frac{HE}{D_p} \tag{1}$$

If $Pe > 1$ then accumulation of particles and skin formation is likely to occur. The values of H, E and D_p can be estimated either from experimental results or derived from the Stokes-Einstein equation. For all formulations, the volume fraction of latex particles to water is approximately 50%, and the particle diameters are approximately 225 nm. The height of the film before drying can thus be assumed to be twice that of the final film thickness. The evaporation rate can be estimated from the gradient of the fast drying region from Figure 2 as the concentration of water is proportional to the integrated absorbance. The Stokes-Einstein equation models diffusion of spherical particles and is given by:

$$D_p = \frac{k_B T}{6\pi\eta r_p} \tag{2}$$

In Equation 2, k_B is the Boltzmann constant, T is the temperature and η is the dynamic viscosity of water. The diffusion coefficient of the latex particles is approximately $2.2 \times 10^{-12}\,m^2s^{-1}$ and thus a typical Peclet number would be 5 for this system at the start of drying, thus being in a region where accumulation of particles and skin formation is likely.

Although with ATR it is not possible to see through the whole thickness of the film, it offers insights into processes occurring at the substrate. For example, in Figure 2, the polymer curve appears to dip at 15 seconds. This may be due to particle migration caused by Brownian motion, where particles migrating to the surface are trapped in the upper layer as they coalesce. It was found by Zang et al[32] studying latex clay coatings, that if heating is

applied soon after coating, latex particles migrate to the surface. Conversely, if the coating is left to dry at room temperature for a time before being dried in an oven, the latex particles become immobilized with the other clay particles as the water slowly evaporates and thus during fast drying, the particles do not move. In this work, there are no other particles and drying occurs quickly after deposition, hence it is expected that particles will migrate to the surface and become trapped as they form part of the skin. The high Peclet number in this work predicts the formation of a skin and after an initial high rate of evaporation, the latex particles pack and sinter together, slowing further evaporation (Figure 3). In the evanescent field, the water cannot leave the film easily, hence the appearance of a plateau. After the formation of a skin or film, pores within the film would close due to polymer chain interdiffusion. The rate at which this occurs depends on the glass transition temperature (T_g) and for thin films, it is envisioned that water would evaporate quickly through the pores before they close. However, the rate of polymer chain interdiffusion would still have an effect on water evaporation even for thin films as pores would close at different rates. For dispersions with a low T_g, polymer chains interdiffuse faster than dispersions with high T_g, causing a slowing of water evaporation.[33] For films with high T_g, though water would evaporate quickly, a porous or cracked film can result.

Materials

All latex dispersions were supplied by BASF and were based on nButylacrylate (nBA) or Ethylhexylacrylate (EHA), with the addition of acrylic acid (AA) and in cases, methylmethacrylate (MMA) as comonomers. The particle sizes of all formulations were approximately 220 nm, pH between 6.2 and 7.3 and solid volume fraction of approximately 50%.

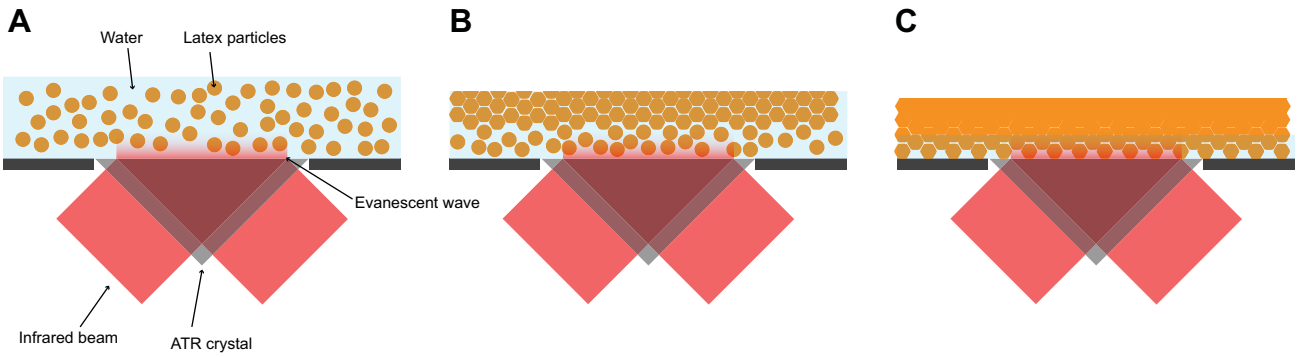

Figure 3: Schematic of high-speed drying of a latex dispersion on an ATR crystal. At the start of drying (A), latex particles are evenly dispersed in water but aggregate at the top surface as water evaporates faster than the particles can diffuse (B). Particles at the surface (C) deform and sinter together, hindering evaporation of the remaining water, giving rise to slower drying. As drying progresses, the concentration of latex particles within the evanescent wave increases (B) and the remaining water at the onset of slow drying (C) within the evanescent wave cannot evaporate as quickly due to skin formation.

Results and discussion

Drying of water containing silica nanoparticles

To demonstrate the effect of non-interacting or non-sintering particles on drying and assess experimental reproducibility, silica nanoparticles of diameter 100 nm were suspended in distilled water at 50% (v/v) and dried according to the specified method. Figure 4 shows the results from three experimental runs and the images of silica and water from all three experiments. The water in all cases dries similarly and there is no slow region as the particles do not sinter together or release adsorbed or absorbed water. The images, generated from integration of the band between 1122 and 1022 cm^{-1}, show that at the end of drying, the silica nanoparticles are pulled away from the centre due to surface tension producing a non-uniform film. The drying profiles, which were generated from averaged pixels of the integrated absorbance images, demonstrate what would be observed with a single element detector and do not show the inhomogeneous drying as seen in the images. From this, the absorbance of the spectral band of silica appears to decrease but this is only because the particles are moving out of the field of view, leaving voids which are also averaged when gen-

erating the drying curve. With imaging, it is possible to selectively mask out these regions so as to average only regions containing silica.

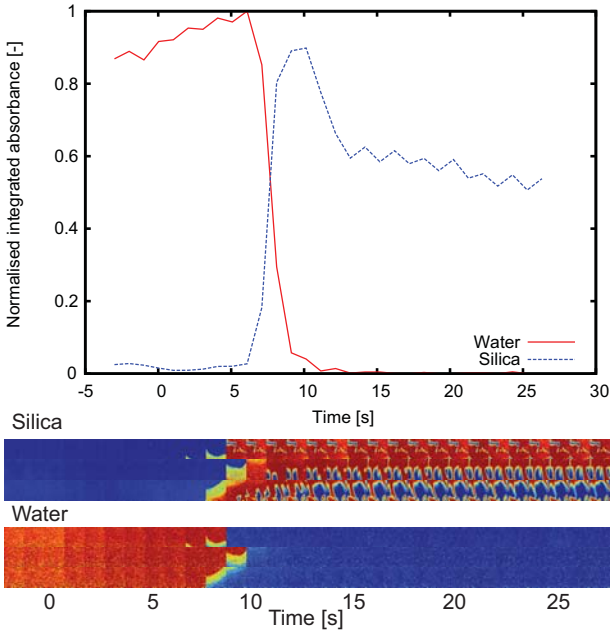

Figure 4: Averaged drying profiles of the silica nanoparticles and water, and integrated absorbance images of silica and water.

Effect of glass transition temperature (T_g)

As previously reported, polymer particles with high T_g will not sinter together upon drying below the MFFT, and form cracked or powdery films. Conversely, dispersions with low T_g drying above the MFFT will sinter together sooner during drying and could give rise to skin formation which would hinder further drying. In this experiment, two dispersions with glass transition temperatures approximately 41 °C and 20 °C were dried. The glass transition temperature was altered by controlling the percentage MMA in the formulations from 45% nBA (T_g calculated to be 20.3 °C) to 32% (T_g calculated to be 40.6 °C). The images in Figure 5 show that for the film with high T_g, a cracked film is formed whereas the other dispersion produced a more uniform film. The drying curves for the films with high T_g have hardly any slow drying region as the large cracks provide paths for water to evaporate in contrast to

the low T_g dispersion, where a slow drying region is clearly visible and the film is uniform. For the low T_g formulations, no plateau is observed in the slow drying region indicating that water was not trapped strongly in this formulation. The polymer curve and images for the high T_g are scaled on a different basis to the others. This is due to the inhomogeneity of the final film and normalisation, which would usually occur based on maximum and minimum integrated absorbance values averaged over the image (valid for homogeneous films), would not apply in this case. As before, selected pixel masking could be used to account for the inhomogeneity, allowing the normalisation to function properly. Here, the curve is presented to indicate the problem with inhomogeneous films and use of a single element detector, which would produce a similar result. It is interesting to see that the curve reaches a minimum at the 12 second mark, likely due to particle movement during drying. This trapping effect[32] could be more pronounced for high T_g films, as the surface temperature is likely to be high enough for partial sintering to occur while particles below the surface can freely migrate to this top layer to be trapped. A skin does not form in this case and the averaging effect as in the previous section causes the final integrated absorbance to be low due to the presence of voids. Both this and the previous section show that with spectroscopic imaging, it's possible to assess the quality of film formation and ascertain the cause of erratic drying curves due to inhomogeneity.

Effect of film thickness

Drying rates can be influenced by film thickness as thin films would dry quickly due to the smaller mass and heat transfer distances. In these experiments, the final film thickness is reported rather than the initial film thickness and as all experiments contained the same volume fraction of solids, the final film thickness can be used as a basis for comparison. For this purpose, a dispersion with a T_g of $-32.6\,^{\circ}\mathrm{C}$ (calculated) was used (monomer composition 89% nBA, 10% MMA, 1% AA with NH_3 added afterwards to bring the pH to 8.5). As shown in Figure 6, the total drying time increases as film thickness increases but the effects of thicker

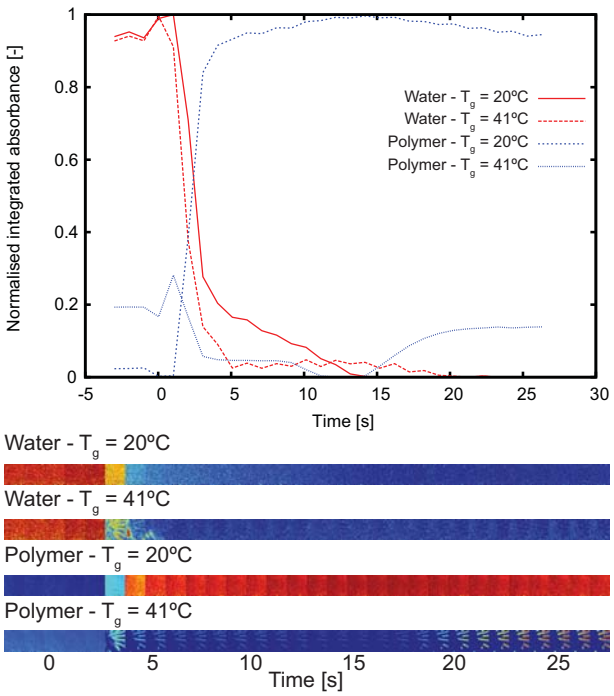

Figure 5: Drying profiles of latex films with high (41 °C) and low (20 °C) glass transition temperatures with example images showing homogeneous drying for the film with low T_g and cracked film formation for film with high T_g.

films are more pronounced in the slow drying region (the length of the plateau and the overall magnitude of t_{slow}), with the fast drying region not being as greatly affected. With thicker films, more water will be trapped to produce the plateau, and the thicker film will also hinder water evaporation compared with thinner films. It is also possible that the rate of pore closure is a factor, where for thin films, water would evaporate before polymer chains interdiffuse significantly (the diffusion coefficient of the polymer chains being the determining factor). The fast drying region is generally less affected as the particles would not have yet aggregated or sintered together as much, except in the case of thicker films where at the surface, this would start to happen more significantly, affecting also this region.

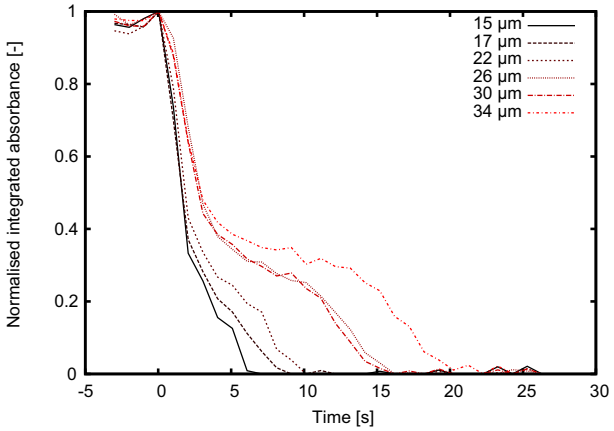

Figure 6: Drying profiles of the same latex dispersion with different final thicknesses.

Using the quantities defined previously (fraction of water remaining and t_{slow}), the effect of film thickness can be plotted against these variables for more quantitative analysis. Figure 7 shows plots of film thickness against the fraction of water remaining and value of t_{slow} respectively.

The effect of doubling the film thickness increases the fraction of remaining water by approximately 12%, and the slow drying regime extends by approximately ten seconds. These results show that with high-speed imaging, drying of even thin films (¡20 µm) can be studied, and that the thickness has a large effect on the slow drying region. It appears that for very thin films (¡15 µm) of this formulation, the plateau region could disappear

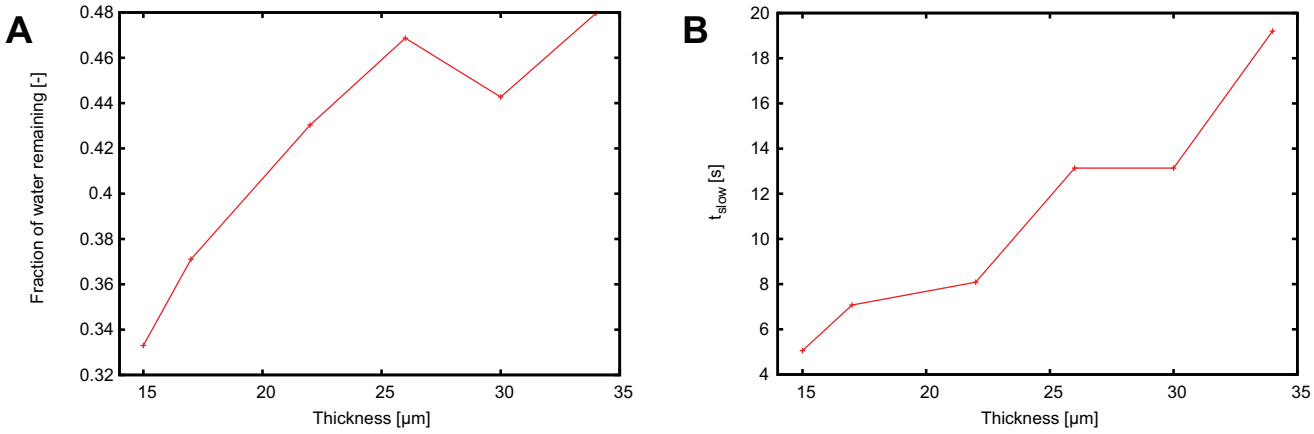

Figure 7: Final film thickness plotted against A) the fraction of water remaining at the onset of slow drying and B) t_{slow}.

completely.

Effect of nBA vs. EHA and % MMA

The main monomers, 2-ethylhexylacrylate (EHA) and nButylacrylate (nBA) were compared along with differing amounts of comonomer, methylmethacrylate (MMA) at 0%, 5% and 10% fractions. Acrylic acid (1%) was present in all formulations and a summary of these, along with their T_g values, is shown in Table 1. Films whose final thicknesses were between 20 and 24 µm were chosen for this study. The EHA and nBA monomers are structurally similar apart from the ethyl side-chain in EHA, making the EHA based formulations more hydrophobic than nBA and this difference appears to cause pronounced differences in the drying characteristics. Plotting the slow drying time against the fraction of water remaining highlights the best formulation for drying as an ideal formulations would occupy the lower left of the graph. This is shown in Figure 8 which are based on an average of four experimental runs. The error bars are higher for the nBA formulations as spreading to form a flat film was more difficult due to the dispersion's higher viscosity. The importance of consistent film thickness when comparing formulations is apparent as shown in the previous section, as thickness variations are a significant source of error between measurements. It is clear that

the addition of methylmethacrylate significantly improves the drying characteristics of both formulations due to the hydrophilic effect of the MMA. Figure 9 shows the drying curves from these experiments, where it is clear that the addition of MMA improves the drying characteristics of both EHA and nBA formulations. It can also be seen that EHA formulations have lower fractions of water remaining, potentially due to its lower hydrophilicity, but extended slow drying times, such that they dry overall more slowly than the nBA formulations. This would indicate formation of a less permeable film for water evaporation once the particles sinter together, compared with the nBA formulations where at the onset of slow drying, the water can still permeate. The T_g of the dispersions also increases with the addition of MMA, which has been shown to decrease the drying time[33] as the films with higher T_g do not coalesce as quickly as those with low T_g. These observations are consistent with those reported for high and low T_g dispersions and while it is not possible to view directly the porosity of the film using ATR-FTIR imaging, SEM images indicate that films with higher T_g retain some of their porosity even after drying, taking much longer for particle deformation and chain interdiffusion.[34,35] It is also known that the colloidal stability is affected by the presence of MMA, and higher colloidal stability leads to less wet sintering and thus faster drying.[36]

Table 1: Table of latex compositions used to study the effects of nBA, EHA and MMA on drying characteristics.

Monomer % composition	T_g [°C] (calculated)
99EHA/1AA	-57.0
94EHA/5MMA/1AA	-52.2
89EHA/10MMA/1AA	-47.2
99nBA/1AA	-42.0
94nBA/5MMA/1AA	-37.4
89nBA/10MMA/1AA	-32.6

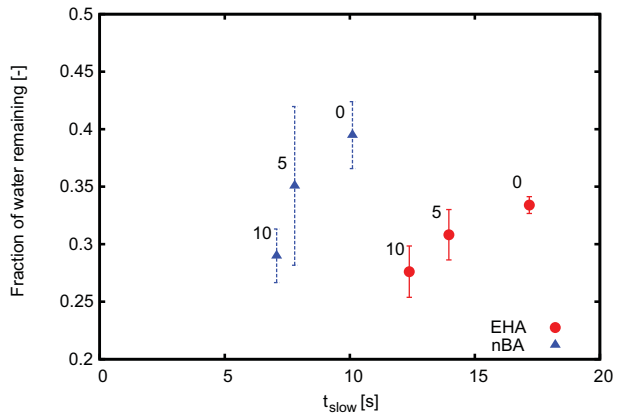

Figure 8: t_{slow} plotted against the fraction of water remaining for both nBA and EHA formulations, with differing amounts of methylmethacrylate in each formulation. The numbers adjacent to the data points indicate the percentage of methylmethacrylate. Error bars are the standard error based on 4 measurements.

Conclusions

The study of fast-drying thin films has been achieved with spectroscopic imaging, demonstrating its applicability to these systems. The use of kinetic-mode (scans without coaddition) allows for the high-speed acquisition of spectral data-cubes which can then be further processed to extract information about the drying of the film. The observed drying curves are consistent with current theoretical understanding and further improvements in this area such as modelling drying films and how the evanescent wave would observe various phenomena would improve the information available using this method.

The drying of silica nanoparticles demonstrated the drying characteristics of particles which do not sinter together during drying unlike latex particles. As the silica nanoparticles were mobile throughout the entire drying process, they agglomerated due to the capillary forces of the remaining water evaporating. The higher T_g (41 °C) dispersion exhibited cracking compared to the film with lower T_g (20 °C), indicating that the particles could not sinter together as the water evaporated. FTIR imaging observed this cracking phenomena which would not have been observed as easily using single-element spectroscopic detection methods. The film thickness dramatically affected drying times, especially in the slow-drying region,

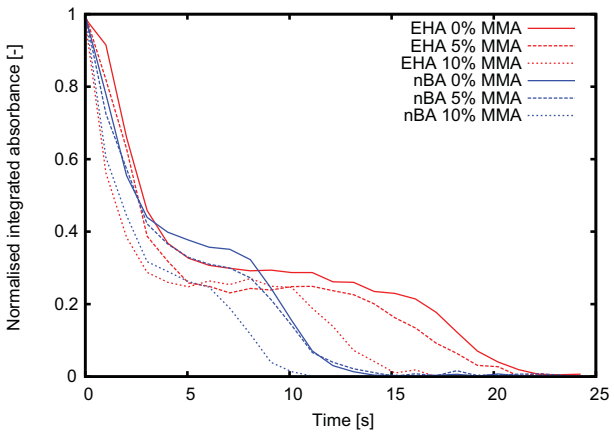

Figure 9: Average drying curves for the 2-ethylhexylacrylate (EHA) and nButylacrylate (nBA) formulations containing differing amounts of methylmethacrylate (MMA) in each formulation.

highlighting the importance of even spreading and thickness control for reproducibility. Finally, the effect of using nBA instead of EHA has a marked effect on the drying kinetics, as does the addition of MMA comonomer. EHA retained less water at the onset of slow drying but had longer slow-drying time compared with nBA formulations, which exhibited a high fraction of water remaining but a shorter slow drying time. This is likely due to the higher hydrophobicity of EHA, which would reduce the fraction of water remaining but with a lower T_g than nBA, would coalesce faster, producing a longer slow-drying time. The effect of MMA lowered both the slow drying time and fraction of water remaining for the formulations, as it would decrease the hydrophobicity but increase the T_g and colloidal stability, causing slower coalescence and allowing faster water evaporation. Comparing these results with the high and low T_g formulations shows that with a large fraction of MMA, the T_g can be raised substantially, giving a drying curve with no plateau. This would indicate that when the film is formed, it would still contain open pores, allowing water to escape easily.

In conclusion, the study of fast film drying has been successfully studied using "kinetic mode" ATR-FTIR spectroscopic imaging for the first time. Physical parameters such as film thickness and the glass transition temperature were studied along with formulation parameters. Fast imaging revealed two stages of drying of latex films, as is consistent in

literature, and further analysis of the drying curves allows relationships to be established between physical/formulation parameters and their effects on different drying regimes. High-speed ATR-FTIR imaging could thus be applied to a wide range of thin-film systems where rapid mass transfer occurs, allowing formulations to be studied under industrially relevant conditions which could lead to more effective formulation optimisation.

Acknowledgements

S.G. Kazarian acknowledges support from the EPSRC grant no. EP/L020564/1. We acknowledge the help and advice from Professor Joe Keddie from the University of Surrey, United Kingdom.

References

(1) Chern, C. Emulsion polymerization mechanisms and kinetics. *Prog. Polym. Sci.* **2006**, *31*, 443–486.

(2) Lovell, P.; El-Aasser, M. *Emulsion polymerization and emulsion polymers*; J. Wiley, 1997.

(3) Routh, A. F. Drying of thin colloidal films. *Rep. Prog. Phys.* **2013**, *76*, 046603–.

(4) Keddie, J. L.; Routh, A. F. In *Fundamentals of Latex Film Formation*; Pasch, H., Ed.; Springer Netherlands, 2010.

(5) Steward, P.; Hearn, J.; Wilkinson, M. An overview of polymer latex film formation and properties. *Adv. Colloid Interface Sci.* **2000**, *86*, 195–267.

(6) Keddie, J. L. Film formation of latex. *Mater. Sci. Eng., R* **1997**, *21*, 101–170.

(7) Ma, Y.; Davis, H.; Scriven, L. Microstructure development in drying latex coatings. *Prog. Org. Coat.* **2005**, *52*, 46–62.

(8) Donald, A. M.; He, C.; Royall, C.; Sferrazza, M.; Stelmashenko, N. A.; Thiel, B. L. Applications of environmental scanning electron microscopy to colloidal aggregation and film formation. *Colloids Surf., A* **2000**, *174*, 37–53.

(9) Bogner, A.; Thollet, G.; Basset, D.; Jouneau, P.-H.; Gauthier, C. Wet STEM: A new development in environmental SEM for imaging nano-objects included in a liquid phase. *Ultramicroscopy* **2005**, *104*, 290–301.

(10) Rottstegge, J.; Traub, B.; Wilhelm, M.; Landfester, K.; Heldmann, C.; Spiess, H. W. Investigations on the Film-Formation Process of Latex Dispersions by Solid-State NMR Spectroscopy. *Macromol. Chem. Phys.* **2003**, *204*, 787–802.

(11) Mallégol, J.; Bennett, G.; McDonald, P. J.; Keddie, J. L.; Dupont, O. Skin Development during the Film Formation of Waterborne Acrylic Pressure-Sensitive Adhesives Containing Tackifying Resin. *J. Adhes.* **2006**, *82*, 217–238.

(12) Wallin, M.; Glover, P. M.; Hellgren, A.-C.; Keddie, J. L.; McDonald, P. J. Depth Profiles of Polymer Mobility during the Film Formation of a Latex Dispersion Undergoing Photoinitiated Cross-Linking. *Macromolecules* **2000**, *33*, 8443–8452.

(13) Ludwig, I.; Schabel, W.; Kind, M.; Castaing, J.-C.; Ferlin, P. Drying and film formation of industrial waterborne latices. *AIChE J.* **2007**, *53*, 549–560.

(14) Guigner, D.; Fischer, C.; Holl, Y. Film Formation from Concentrated Reactive Silicone Emulsions. 1. Drying Mechanism. *Langmuir* **2001**, *17*, 3598–3606.

(15) Zhang, Q.-N.; Zhang, Y.; Cai, C.; Guo, Y.-C.; Reid, J. P.; Zhang, Y.-H. In Situ Observation on the Dynamic Process of Evaporation and Crystallization of Sodium Nitrate Droplets on a ZnSe Substrate by FTIR-ATR. *J. Phys. Chem. A* **2014**, *118*, 2728–2737.

(16) Zhao, C.; Holl, Y.; Pith, T.; Lambla, M. FTIR-ATR spectroscopic determination of the distribution of surfactants in latex films. *Colloid Polym. Sci.* **1987**, *265*, 823–829.

(17) Niu, B.-J.; Urban, M. W. Recent advances in stratification and film formation of latex films; attenuated total reflection and step-scan photoacoustic FTIR spectroscopic studies. *J. Appl. Polym. Sci.* **1998**, *70*, 1321–1348.

(18) Chattopadhyay, R.; Bousfield, D. W.; Tripp, C. P. ATR-IR spectroscopy for dynamically measuring the effect of drying on binder migration. *Proc. 12th TAPPI Advanced Coating Fundamentals Symposium* **2012**, 239–249.

(19) Kimber, J. A.; Kazarian, S. G. Macro ATR-FTIR Spectroscopic Imaging of Dynamic Processes. *Spectroscopy* **2014**, *29*, 34–44.

(20) Kazarian, S. G.; Ewing, A. V. Applications of Fourier transform infrared spectroscopic imaging to tablet dissolution and drug release. *Expert Opin. Drug Delivery* **2013**, *10*, 1207–1221.

(21) Kazarian, S. G.; Chan, K. L. A. ATR-FTIR spectroscopic imaging: recent advances and applications to biological systems. *Analyst* **2013**, *138*, 1940–1951.

(22) Glassford, S.; Chan, K. L. A.; Byrne, B.; Kazarian, S. G. Chemical Imaging of Protein Adsorption and Crystallization on a Wettability Gradient Surface. *Langmuir* **2012**, *28*, 3174–3179.

(23) Frosch, T.; Chan, K. L. A.; Wong, H. C.; Cabral, J. T.; Kazarian, S. G. Nondestructive Three-Dimensional Analysis of Layered Polymer Structures with Chemical Imaging. *Langmuir* **2010**, *26*, 19027–19032.

(24) Kazarian, S. G.; van der Weerd, J. Simultaneous FTIR Spectroscopic Imaging and Visible Photography to Monitor Tablet Dissolution and Drug Release. *Pharm. Res.* **2008**, *25*, 853–860.

(25) Chan, K. L. A.; Tay, F. H.; Poulter, G.; Kazarian, S. G. Chemical Imaging with Variable

Angles of Incidence Using a Diamond Attenuated Total Reflection Accessory. *Appl. Spectrosc.* **2008**, *62*, 1102–1107.

(26) Chan, K. L. A.; Niu, X.; deMello, A. J.; Kazarian, S. G. Generation of Chemical Movies: FT-IR Spectroscopic Imaging of Segmented Flows. *Anal. Chem.* **2011**, *83*, 3606–3609.

(27) Croll, S. G. Drying of Latex Paint. *Journal of Coatings Technology* **1986**, *58*, 41–49.

(28) Vanderhoff, J. W.; Bradford, E. B.; Carrington, W. K. The transport of water through latex films. *J. polym. sci., C Polym. symp.* **1973**, *41*, 155–174.

(29) Taylor, J. W.; Winnik, M. A. Functional latex and thermoset latex films. **2004**, *1*, 163–190.

(30) Kiil, S. Drying of latex films and coatings: Reconsidering the fundamental mechanisms. *Prog. Org. Coat.* **2006**, *57*, 236–250.

(31) Eckersley, S.; Rudin, A. Drying behavior of acrylic latexes. *Prog. Org. Coat.* **1994**, *23*, 387–402.

(32) Zang, Y.-H.; Du, J.; Du, Y.; Wu, Z.; Cheng, S.; Liu, Y. The Migration of Styrene Butadiene Latex during the Drying of Coating Suspensions: When and How Does Migration of Colloidal Particles Occur? *Langmuir* **2010**, *26*, 18331–18339.

(33) Carter, F. T.; Kowalczyk, R. M.; Millichamp, I.; Chainey, M.; Keddie, J. L. Correlating Particle Deformation with Water Concentration Profiles during Latex Film Formation: Reasons That Softer Latex Films Take Longer to Dry. *Langmuir* **2014**, *30*, 9672–9681.

(34) Gonzalez, E.; Tollan, C.; Chuvilin, A.; Barandiaran, M. J.; Paulis, M. Determination of the Coalescence Temperature of Latexes by Environmental Scanning Electron Microscopy. *ACS Appl. Mater. Interfaces* **2012**, *4*, 4276–4282.

(35) Keddie, J. L.; Meredith, P.; Jones, R. A. L.; Donald, A. M. Kinetics of Film Formation in Acrylic Latices Studied with Multiple-Angle-of-Incidence Ellipsometry and Environmental SEM. *Macromolecules* **1995**, *28*, 2673–2682.

(36) Erkselius, S.; Wads, L.; Karlsson, O. J. Drying rate variations of latex dispersions due to salt induced skin formation. *J. Colloid Interface Sci.* **2008**, *317*, 83–95.